A 3D MIXED FINITE-ELEMENT APPROXIMATION OF THE SEMICONDUCTOR ENERGY-TRANSPORT EQUATIONS*

STEPHAN GADAU† AND ANSGAR JÜNGEL‡

Abstract. The stationary energy-transport equations for semiconductors in three space dimensions are numerically discretized. The physical variables are the electron density, the energy density, and the electric potential. Physically motivated mixed Dirichlet-Neumann boundary conditions are employed. The numerical approximation is based on an hybridized mixed finite-element method using Raviart-Thomas elements, applied to the dual-entropy formulation of the energy-transport model. For the solution of the nonlinear discrete system, a Newton scheme with adaptive potential stepping and two decoupling Gummel-type strategies with reduced rank extrapolation are proposed. Multi-gate field-effect transistors in 2D and 3D are numerically simulated.

Key words. Energy-transport equations, dual entropy variables, cross-diffusion system, mixed finite elements, Raviart-Thomas elements, decoupled iteration scheme, multi-gate MESFET.

AMS subject classifications. 65N30, 82D37, 80A20.

1. Introduction. The production of actual semiconductor devices is mainly based on a planar technology. The down-scaling of the devices, however, leads to severe problems, like an increase of the power density and noise effects. A possible solution to reduce the noise is the use of multi-gate field-effect transistors in which the gate contact encloses the channel region from different sides, leading to smaller no-signal currents. Such devices have to be usually modeled in three space dimensions. In order to avoid thermal effects like hot spots, the devices need to be simulated by transport equations involving the particle temperature as an independent variable. A model which satisfies this requirement are the energy-transport equations. In this paper, we present for the first time a mixed finite-element approximation of the stationary energy-transport equations in three space dimensions for the simulation of multi-gate field-effect transistors.

The (scaled) stationary energy-transport equations for the electron density n, the electron energy density e, and the electric potential V read as follows [24]:

$$-\operatorname{div} J_n = 0, \quad J_n = \nabla n - \frac{n}{T}\nabla V, \tag{1.1}$$

$$-\operatorname{div} J_e = -J_n \cdot \nabla V + W(n,T), \quad J_e = \frac{3}{2}(\nabla(nT) - n\nabla V), \tag{1.2}$$

$$\lambda^2 \Delta V = n - C(x), \tag{1.3}$$

where J_n is the particle current density, J_e the energy current density, $e = \frac{3}{2}nT$ the energy density with the electron temperature T, $C(x)$ the doping concentration characterizing the device, $W(n,T) = \frac{3}{2}n(T-T_0)/\tau_0$ the relaxation term with the lattice temperature T_0 and the relaxation time τ_0, and λ is the scaled Debye length.

*The second author has been partially supported by the Wissenschaftskolleg "Differential Equations", funded by the Fonds zur Förderung der wissenschaftlichen Forschung (FWF), by the FWF project P20214-N16, and by the Deutsche Forschungsgemeinschaft, grant JU359/7. The authors thank Prof. Paola Pietra (Pavia, Italy) for fruitful discussions. This research is part of the ESF program "Global and geometrical aspects of nonlinear partial differential equations (GLOBAL)".

†Institut für Mathematik, Universität Mainz, Staudingerweg 9, 55099 Mainz, Germany; e-mail: gadau@mathematik.uni-mainz.de.

‡Institut für Analysis und Scientific Computing, Technische Universität Wien, Wiedner Hauptstr. 8-10, 1040 Wien, Austria; e-mail: juengel@anum.tuwien.ac.at.

The equations are solved in a bounded domain $\Omega \subset \mathbb{R}^3$ and are complemented by the physically motivated boundary conditions

$$n = n_D, \quad T = T_D, \quad V = V_D \quad \text{on } \Gamma_D, \tag{1.4}$$

$$J_n \cdot \nu = J_e \cdot \nu = \nabla V \cdot \nu = 0 \quad \text{on } \Gamma_N, \tag{1.5}$$

modeling the contacts Γ_D and the insulating boundary parts Γ_N, where $n_D > 0$ and $T_D > 0$. We have assumed that $\partial\Omega = \Gamma_D \cup \Gamma_N$, $\Gamma_D \cap \Gamma_N = \emptyset$ and that the exterior normal unit vector ν exists a.e. on $\partial\Omega$.

The first energy-transport model was presented by Stratton in 1962 [34]. The model can be derived from the semiconductor Boltzmann equation by means of the Hilbert expansion method [4]. The derivation of (1.1)-(1.2) assumes parabolic energy bands and nondegenerate Boltzmann statistics [14]. A rigorous derivation can be found in [5].

In the mathematical literature, there are only a few results concerning the existence and uniqueness of solutions to (1.1)–(1.5), due to difficulties coming from the strong coupling and the lack of a maximum principle. Existence of weak solutions for the transient or stationary equations was proved in near-equilibrium situations or for special diffusion coefficients only [12, 13, 15, 19].

The numerical discretization of energy-transport models was investigated in the physical literature for quite some time, see, e.g., [2, 11, 17, 33]. Mathematicians started to pay attention to these models in the 1990s, using essentially nonoscillatory numerical schemes [23], finite-difference methods [29], mixed finite-volume schemes [6], or mixed finite-element techniques [10, 14, 20, 21, 27] (see also [8] for an overview). An essential advantage of the mixed finite-element discretization is the "current conservation", i.e., the normal component of the discrete current density is continuous across inter-element boundaries [7].

The finite-element approximation of the 2D energy-transport model in [20, 21] is based on the observation that the energy-transport equations (1.1)-(1.2) are given in drift-diffusion form, which allows to use well-understood discrete schemes developed originally for the drift-diffusion model [9]. On the other hand, the drift-diffusion formulation (1.1)-(1.2) involves dominant convective terms in case of high electric fields, and special discretization techniques become necessary in order to maintain the positivity-preserving property of the scheme [25, 26].

This disadvantage can be avoided by using a formulation of the equations in terms of the dual entropy variables $w_1 = (\mu - V)/T$ and $w_2 = -1/T$, where the chemical potential μ relates to the electron density by $n = T^{3/2}e^{\mu/T}$. In these variables, the convective parts involving the electric field $-\nabla V$ disappear and the system (1.1)-(1.2) becomes symmetric:

$$-\operatorname{div} I_1 = 0, \quad -\operatorname{div} I_2 = W, \quad I_i = D_{i1}\nabla w_1 + D_{i2}\nabla w_2, \quad i = 1, 2, \tag{1.6}$$

where the diffusion coefficients D_{ij} are given by

$$D_{11} = n, \quad D_{12} = D_{21} = -\Big(V + \frac{3}{2w_2}\Big)n, \quad D_{22} = \Big(\Big(V + \frac{3}{2w_2}\Big)^2 + \frac{3}{2w_2^2}\Big)n,$$

and the electron density $n = (-w_2)^{-3/2}e^{w_1 - Vw_2}$ can be written as a function of V, w_1, and w_2. This formulation was the basis of analytical studies [12, 19] and numerically discretized in one space dimension in [27]. Notice that the diffusion matrix $\boldsymbol{D} = (D_{ij})$

is symmetric and positive definite (if $n > 0$ and $T > 0$) and that (1.6) becomes an elliptic cross-diffusion system.

In this paper, we discretize the three-dimensional energy-transport equations in the dual-entropy formulation (1.3)-(1.6) using Raviart-Thomas finite elements. In order to reduce the number of variables in the mixed-hybrid formulation, we employ static condensation as in [20]. The resulting nonlinear algebraic system is solved by three different iterative schemes.

The first scheme is based on the full Newton method with a continuation in the applied voltage, i.e., the solution of the previous voltage U is used as the initial guess in the Newton method to compute the solution with applied voltage $U + \triangle U$. Usually, the voltage step $\triangle U$ is chosen constant during the iterations [20, 21]. Here, we implement a path-following algorithm in order to allow for adaptive voltage steps.

The Newton method has the drawbacks that a large linear system has to be solved in each step, which is numerically expensive, and that it is unflexible with respect to changes of the model. Therefore, the second and third iteration schemes are concerned with decoupling strategies of Gummel type, which are easy to implement and easy to modify. Moreover, in contrast to the Jacobian coming from the Newton method, the diffusion matrix remains symmetric and positive definite during the iterations, such that efficient linear solvers can be used. The Gummel method can be regarded as an approximate Newton method, where the information about the strong coupling of the unknowns is incorporated into the Poisson equation (1.3), and the Jacobian of the system is replaced by a diagonal matrix [22].

The idea of the first decoupling is as follows. We write the diffusion matrix $\mathbf{D}$ as $\boldsymbol{M} - \mathbf{N}$, where

$$\boldsymbol{M} = n \begin{pmatrix} 1 & -(V + \frac{3}{2} w_2^{-1}) \\ -(V + \frac{3}{2} w_2^{-1}) & (V + \frac{3}{2} w_2^{-1})^2 + \frac{3}{2}(1+\alpha) w_2^{-2} \end{pmatrix}, \ \boldsymbol{N} = n \begin{pmatrix} 0 & 0 \\ 0 & \frac{3}{2} \alpha w_2^{-2} \end{pmatrix}, \tag{1.7}$$

and α is some nonnegative parameter. This formulation has the effect that it increases the "ellipticity" of the system in the sense that the determinant of $\boldsymbol{M}$ becomes larger. The iteration matrix, which would correspond to a linear algebraic system, reads as

$$\boldsymbol{I} = \boldsymbol{M}^{-1} \boldsymbol{N} = \frac{\alpha}{1+\alpha} \begin{pmatrix} 0 & V + \frac{3}{2} w_2^{-1} \\ 0 & 1 \end{pmatrix}.$$

Hence, we expect that large values of α entail slow convergence. In order to improve the convergence property, we combine the decoupled scheme with a reduced rank extrapolation method.

In the above Gummel-type scheme, the current continuity equations (1.6) are still coupled. In order to achieve a completely decoupled system, we propose a second Gummel-type iteration. The idea consists in a decoupling of the current continuity equations by backward substitution, which corresponds to a nonlinear Gauß-Seidel iteration for the entire system. More precisely, we rewrite (1.6) as

$$-\operatorname{div} I_1 = 0, \qquad I_1 = D_{11} \nabla w_1 + D_{12} \nabla w_2, \tag{1.8}$$

$$-\operatorname{div} \widetilde{I}_2 = \frac{W}{1+\alpha} - \frac{3}{2} \frac{\alpha}{1+\alpha} \operatorname{div}(n w_2^{-2} \nabla w_2), \quad \widetilde{I}_2 = \frac{D_{21}}{1+\alpha} \nabla w_1 + \widetilde{D}_{22}(\alpha) \nabla w_2, \tag{1.9}$$

where $\widetilde{I}_2 = I_2/(1+\alpha)$ and $\widetilde{D}_{22}(\alpha) = n(1+\alpha)^{-1}(V + \frac{3}{2} w_2^{-1})^2 + \frac{3}{2} n w_2^{-2}$. For large values of α, we have reduced coupling and the new diffusion matrix is "almost" triangular if α is large, since then, $D_{21}/(1+\alpha)$ is small compared to one. It turns out that the

completely decoupled Gummel iteration scheme together with the vector extrapolation technique leads to an algorithm which converges superlinearly.

The paper is organized as follows. In section 2 we describe the finite-element discretization and the static condensation. Moreover, the evaluation of the terminal particle current is explained. Section 3 is concerned with the iteration schemes and some details of the implementation. In section 4 we simulate various MESFET (metal-semiconductor field-effect transistor) devices in 2D and 3D. We conclude in section 5.

2. Numerical approximation. In this section we describe the finite-element discretization of the energy-transport system (1.6) and the iterative methods.

2.1. Mixed finite-element discretization. We discretize (1.3) and (1.6) employing Raviart-Thomas finite elements. Let $\Omega \subset \mathbb{R}^3$ be a polyhedral domain and let $(\mathcal{T}_h)$ be a regular family of simplicial finite-element partitions of tetrahedra of Ω. Furthermore, we denote by $\mathcal{E}_h$ the set of all faces of the elements of $\mathcal{T}_h$, by $\mathcal{E}_h'$ the set of all inner faces, and by $\mathcal{E}(\Gamma_D)$ the set of all faces lying on the Dirichlet boundary. We assume here that Γ_D consists only of faces of elements in $\mathcal{T}_h$. Finally, we set $\mathcal{E}(K) = \{S \in \mathcal{E}_h : S \subset \partial K\}$ for $K \in \mathcal{T}_h$.

For a given element $K \in \mathcal{T}_h$, we introduce the following (local) vector-valued approximation space for the current densities:

$$\Sigma(K) = \text{span}\{(1,0,0)^\top, (0,1,0)^\top, (0,0,1)^\top, (x-x_s, y-y_s, z-z_s)^\top\},$$

where $(x_s, y_s, z_s)^\top$ denotes the barycenter of K. The global ansatz space is

$$X_h = \{\tau \in L^2(\Omega)^3 : \tau_{|K} \in \Sigma(K)\ \forall K \in \mathcal{T}_h\}.$$

The hybridization procedure involves two different approximation spaces for w_i,

$$Y_h = \{\phi \in L^2(\Omega) : \phi_{|K} = \text{const.}\ \forall K \in \mathcal{T}_h\},$$
$$Z_{h,\xi} = \Big\{\mu \in L^2(\cup_{S\in\mathcal{E}_h} S) : \mu_{|S} = \text{const.}\ \forall S \in \mathcal{E}_h, \int_S (\mu - \xi)\,ds = 0\ \forall S \in \mathcal{E}(\Gamma_D)\Big\},$$

where $\xi \in L^2(\Gamma_D)$. These spaces represent a hybridized version of the mixed finite-element method with Raviart-Thomas elements of lowest order [28].

We present the mixed-hybrid formulation of the current continuity equations (1.6). The discretization of the Poisson equation is done in a similar way. For this, we define the inverse (A_{ij}) of the diffusion matrix $\boldsymbol{D} = (D_{ij})$,

$$A_{11} = \frac{2w_2^2}{3n^2} D_{22}, \quad A_{12} = A_{21} = -\frac{2w_2^2}{3n^2} D_{21}, \quad A_{22} = \frac{2w_2^2}{3n^2} D_{11},$$

the electron density as a function of V, w_1, and w_2,

$$n = n(V, w_1, w_2) = (-w_2)^{-3/2} e^{w_1 - V w_2}, \tag{2.1}$$

and the Dirichlet boundary data

$$w_{1D} = \log\Big(\frac{n_D}{T_D^{3/2}}\Big) - \frac{V_D}{T_D}, \quad w_{2D} = -\frac{1}{T_D}. \tag{2.2}$$

The mixed-hybrid formulation of (1.6) is as follows: Find I_{1h}, $I_{2h} \in X_h$, v_{1h}, $v_{2h} \in Y_h$, and $w_{1h} \in Z_{h,w_{1D}}$, $w_{2h} \in Z_{h,w_{2D}}$ such that for all $\tau_i \in X_h$, $\phi_i \in Y_h$, and $\mu_i \in Z_{h,0}$, $i = 1, 2$,

$$0 = \sum_{K\in\mathcal{T}_h} \int_K (A_{i1,K} I_{1h} + A_{i2,K} I_{2h}) \cdot \tau_i \, dx + \int_K v_{ih} \operatorname{div} \tau_i \, dx - \sum_{S\in\mathcal{E}(K)} \int_S w_{ih} \tau_i \cdot \nu \, ds, \tag{2.3}$$

$$0 = \sum_{K\in\mathcal{T}_h} \int_K \operatorname{div} I_{ih} \phi_i \, dx + (i-1) \int_K W_K \phi_i \, dx, \tag{2.4}$$

$$0 = \sum_{K\in\mathcal{T}_h} \sum_{S\in\mathcal{E}(K)} \int_S \mu_i I_{ih} \cdot \nu \, ds. \tag{2.5}$$

Here, we have employed the abbreviations $A_{ij,K} = A_{ij}(V_K, w_{1K}, w_{2K})$ and $W_K = W(V_K, w_{1K}, w_{2K}) = 3n_K(1 + w_{2K}^{-1})/2\tau$, where $n_K = (-w_{2K})^{-3/2} e^{w_{1K} - V_K w_{2K}}$. The functions V_K, w_{1K}, and w_{2K} are defined as follows. Let $|S_i|$ denote the measure of the face S_i of a tetrahedron and let $V_1, \ldots, V_4$ be the nodal values of V_h associated with the faces. Then we set

$$V_K = \frac{|S_1|^2 V_1 + |S_2|^2 V_2 + |S_3|^2 V_3 + |S_4|^2 V_4}{|S_1|^2 + |S_2|^2 + |S_3|^2 + |S_4|^2}.$$

In a similar way, we define w_{1K} and w_{2K}. This choice is motivated from the results of [3]. Instead of averaging over faces, averaging over edges is also possible, and the results differ only slightly.

Eq. (2.3) is a discrete weak version of the last equation in (1.6). The second equation (2.4) corresponds to a discrete version of the first two equations in (1.6). Finally, (2.5) imposes the continuity requirement of $I_{ih} \cdot \nu$ at the inter-element boundaries. It follows from this equation that the mean value of the jump $I_{ih} \cdot \nu$ equals zero, since the test functions μ_i are constant on every face. Hence, conservation of the current densities holds in a weak sense.

Denoting by $\boldsymbol{I}_{ih}$, $\boldsymbol{v}_{ih}$, and $\boldsymbol{w}_{ih}$ the vectors of the nodal values, the nonlinear system associated with the mixed-hybrid formulation is

$$\begin{pmatrix} \boldsymbol{A}_{11} & \boldsymbol{A}_{12} & \boldsymbol{B} & \mathbf{0} & -\boldsymbol{C} & \mathbf{0} \\ \boldsymbol{A}_{21} & \boldsymbol{A}_{22} & \mathbf{0} & \boldsymbol{B} & \mathbf{0} & -\boldsymbol{C} \\ \boldsymbol{B}^\top & \mathbf{0} & \mathbf{0} & \mathbf{0} & \mathbf{0} & \mathbf{0} \\ \mathbf{0} & \boldsymbol{B}^\top & \mathbf{0} & \mathbf{0} & \mathbf{0} & \mathbf{0} \\ \boldsymbol{C}^\top & \mathbf{0} & \mathbf{0} & \mathbf{0} & \mathbf{0} & \mathbf{0} \\ \mathbf{0} & \boldsymbol{C}^\top & \mathbf{0} & \mathbf{0} & \mathbf{0} & \mathbf{0} \end{pmatrix} \begin{pmatrix} \boldsymbol{I}_{1h} \\ \boldsymbol{I}_{2h} \\ \boldsymbol{v}_{1h} \\ \boldsymbol{v}_{2h} \\ \boldsymbol{w}_{1h} \\ \boldsymbol{w}_{2h} \end{pmatrix} = \begin{pmatrix} \mathbf{0} \\ \mathbf{0} \\ \mathbf{0} \\ -\boldsymbol{F} \\ \mathbf{0} \\ \mathbf{0} \end{pmatrix}.$$

The matrices $\boldsymbol{A}_{ij}$, $\boldsymbol{B}$, and $\boldsymbol{C}$ and the vector $\boldsymbol{F}$ correspond to

$$\int_K \tau_i \cdot \tau_j dx, \quad \int_K \operatorname{div} \tau_i \phi_j dx, \quad \int_{\partial K} \tau_i \mu_j ds, \quad \int_K W_K \phi_i dx,$$

respectively, where τ_i, ϕ_i, and μ_i are the basis functions of the respective spaces.

By static condensation, the variables $\boldsymbol{I}_{jh}$ and $\boldsymbol{v}_{jh}$ can be eliminated, and we obtain a nonlinear system acting only on the Lagrange multipliers $\boldsymbol{w}_{1h} = (w_{1i})$ and $\boldsymbol{w}_{2h} = (w_{2i})$. The nodal values of the current densities $\boldsymbol{I}_{1h}$ and $\boldsymbol{I}_{2h}$ can be reconstructed

from $\boldsymbol{w}_{1h}$ and $\boldsymbol{w}_{2h}$ by the formulae

$$(\boldsymbol{I}_{1h})_j = \begin{cases} -\dfrac{D_{11,K}}{|K|}\displaystyle\sum_{i=1}^4 n_{i,j}(w_{1i})_{|S_i} - \dfrac{D_{12,K}}{|K|}\sum_{i=1}^4 n_{i,j}(w_{2i})_{|S_i} & \text{if } j=1,2,3, \\ 0 & \text{if } j=4, \end{cases} \tag{2.6}$$

$$(\boldsymbol{I}_{2h})_j = \begin{cases} -\dfrac{D_{21,K}}{|K|}\displaystyle\sum_{i=1}^4 n_{i,j}(w_{1i})_{|S_i} - \dfrac{D_{22,K}}{|K|}\sum_{i=1}^4 n_{i,j}(w_{2i})_{|S_i} & \text{if } j=1,2,3, \\ \dfrac{1}{3}\dfrac{1}{|K|}W(V_K, w_{1K}, w_{2K}), & \text{if } j=4, \end{cases} \tag{2.7}$$

where we have set $D_{ji,K} = D_{ji}(V_K, w_{1K}, w_{2K})$, $n_{i,j} = |S_i|\nu_{i,j}$, and $\nu_{i,j}$ is the j-th component of the unit vector ν_i.

2.2. Evaluation of the terminal currents. An important output of the device simulations are the fluxes through the Ohmic contacts. In this subsection, we make precise how these fluxes are determined. We proceed similarly as in [16]. Let $c \subset \Gamma_D$ be a contact, separated from the other contacts by a positive distance. The discrete electron current is defined by

$$I_{1,c}^h = \sum_{S\in\mathcal{E}(c)} \int_S I_{1h}\cdot\nu\, ds,$$

where $\mathcal{E}(c) = \{S \in \mathcal{E}_h : S \subset c\}$. The continuity of the normal component of I_{1h} across the inter-element faces allows for an expansion of the above formula, involving all faces. In order to show this, let $\mu_0 \in Z_{h,\xi}$, where $\xi \in L^2(\Gamma_D)$ is such that $\xi(x) = 1$ for $x \in c$ and $\xi(x) = 0$ else. Then

$$\begin{aligned} I_{1,c}^h &= \sum_{S\in\mathcal{E}(c)} \int_S \mu_0 I_{1h}\cdot\nu\, ds = \sum_{S\in\mathcal{E}_h} \int_S \mu_0 I_{1h}\cdot\nu\, ds - \sum_{S\in\mathcal{E}_h'} \int_S \mu_0 I_{1h}\cdot\nu\, ds \\ &= \sum_{S\in\mathcal{E}_h} \int_S \mu_0 I_{1h}\cdot\nu\, ds = \sum_{K\in\mathcal{T}_h}\sum_{S\in\mathcal{E}(K)} \int_S \mu_0 I_{1h}\cdot\nu\, ds. \end{aligned}$$

By means of (2.6) and the fact that μ_0 is piecewise constant on the faces,

$$I_{1,c}^h = -\sum_{K\in\mathcal{T}_h}\Big(\frac{D_{11,K}}{|K|}\sum_{S,\widetilde{S}\in\mathcal{E}(K)}(n_S\cdot n_{\widetilde{S}})w_{1S}\mu_{0\widetilde{S}} + \frac{D_{12,K}}{|K|}\sum_{S,\widetilde{S}\in\mathcal{E}(K)}(n_S\cdot n_{\widetilde{S}})w_{2S}\mu_{0\widetilde{S}}\Big), \tag{2.8}$$

where w_{1S} denotes the value of w_{1h} associated with the face S (similar for $\mu_{0\widetilde{S}}$) and $n_S = |S|\nu_S$ is the scaled outward normal on S. In the numerical tests, we have choosen $\mu_0 \in Z_{h,\xi}$ satisfying $\mu_{0\widetilde{S}} = 0$ if $\widetilde{S} \in \mathcal{E}_h'$. Then (2.8) reduces to

$$I_{1,c}^h = -\sum_{\widetilde{S}\in\mathcal{E}(c)}\mu_{0\widetilde{S}}\sum_{K\in\mathcal{T}_h}\Big(\frac{D_{11,K}}{|K|}\sum_{S\in\mathcal{E}(K)}(n_S\cdot n_{\widetilde{S}})w_{1S} + \frac{D_{12,K}}{|K|}\sum_{S\in\mathcal{E}(K)}(n_S\cdot n_{\widetilde{S}})w_{2S}\Big).$$

3. Iterative schemes. In this section we present the iterative methods employed for the solution of the nonlinear algebraic systems. We introduce three schemes: a Newton method, combined with a path-following technique for the voltage step, and two Gummel-type methods, combined with vector extrapolation.

3.1. Newton method and adaptive voltage stepping. The Newton method is combined with a continuation in the applied voltage. First, the system is solved (by Newton's method) using zero applied bias. Given a solution of the problem with applied voltage U, this solution is taken as an initial guess to solve the problem with applied voltage $U + \triangle U$. Usually, the step size $\triangle U$ is constant. A more advanced strategy is to adjust the step size automatically. This is done by the path-following method which we describe now.

Let the Dirichlet boundary consist of the two contacts $\Gamma_{D,1}$ and $\Gamma_{D,2}$. Furthermore, let V_A be an extension of the applied voltage defined at the contact $\Gamma_{D,1}$ into Ω, given by

$$\Delta V_A = 0 \text{ in } \Omega, \quad V_A = U \text{ on } \Gamma_{D,1}, \quad V_A = 0 \text{ on } \Gamma_{D,2}, \quad \nabla V_A \cdot \nu = 0 \text{ on } \Gamma_N, \quad (3.1)$$

where the voltage is assumed to be constant on the contact. We consider the energy-transport equations (1.6), where V, w_1, and w_2 are replaced by $V_\rho + \rho V_A$, $u_1 + \rho V_A w_2$, and u_2, respectively, where $\rho \in [0,1]$ is a parameter. The transformed system has to be solved for V_ρ, u_1, and u_2. Adapting the Dirichlet boundary conditions appropriately, $V = V_\rho + V_A$, $w_1 = u_1 + V_A u_2$, and $w_2 = u_2$ solves the original problem. We observed in the numerical experiments that this transformation improves the convergence properties.

Let $u = (V_h, u_{1h}, u_{2h})$ be a discrete solution of this system, written as $G(u,\rho) = 0$ for some function G. The solution set $L = \{(u,\rho) : G(u,\rho) = 0\}$ generically consists of one-dimensional paths. In order to approximate the component L_0 of L, which is defined by an initial solution $(u^{(0)}, \rho^{(0)}) \in L$, so-called predictor-corrector path-following methods can be used. For tracing the solution path L_0 of $G(u,\rho) = 0$, we employ the pseudo-arglength method [30]. The successor $(u^{(k+1)}, \rho^{(k+1)})$ to $(u^{(k)}, \rho^{(k)})$ in L_0 is then defined as the solution of

$$G(u,\rho) = 0, \quad (c^{(k)})^\top (u - u^{(k)}) + \gamma^{(k)}(\rho - \rho^{(k)}) = \tau^{(k)}, \quad (3.2)$$

where $\tau^{(k)} > 0$ is a step size and the vectors $c^{(k)}$ and $\gamma^{(k)}$ are chosen such that $(c^{(k)}, \gamma^{(k)})$ is not orthogonal to the one-dimensional kernel of $G'(u^{(k)}, \rho^{(k)})$. The choice of these vectors is made precise in section 3.3.

Then Newton's method is applied to (3.2) in order to solve the energy-transport system and to obtain the parameter ρ. The Jacobian matrix of the entire system is neither symmetric nor definite. Therefore, we use direct elimination to solve the linear systems. By reduction of the band width, the fill-in is reduced.

3.2. Gummel-type methods and vector extrapolation. We propose two Gummel-type methods. The first scheme only decouples the Poisson equation and the linearized current continuity equations are solved in each iteration step as a coupled system. In the second scheme, the two current continuity equations are decoupled such that only linear scalar equations have to be solved in each step. Since Gummel-type iteration procedures have a low convergence rate, we employ a vector extrapolation technique in order to improve the convergence.

The first Gummel-type method is based on the idea to split the diffusion matrix as explained in the introduction (see (1.7)). Splitting the relaxation term in a similar way, the energy-transport equations (1.6) take the form

$$\begin{aligned} -\operatorname{div} I_1 &= 0, & I_1 &= D_{11}\nabla w_1 + D_{12}\nabla w_2, \\ -\operatorname{div} I_2 + \sigma(w_2)w_2 &= W_1(w_2), & I_2 &= D_{21}\nabla w_1 + \Big(D_{22} + \frac{3}{2}\alpha n w_2^{-1}\Big)\nabla w_2, \end{aligned}$$

where

$$\sigma(w_2) = -\frac{3}{2}(1+\alpha)\frac{n}{\tau}w_2^{-1} > 0, \tag{3.3}$$
$$W_1(w_2) = \frac{3}{2}\frac{n}{\tau}(1-\alpha w_2)w_2^{-1} - \alpha\operatorname{div}\Big(\frac{3}{2}nw_2^{-1}\nabla w_2\Big).$$

Notice that we have not renamed the variables. This idea can be used to define the following fixed-point iteration.

Algorithm 1: Assign the starting values $w_1^{(0)}$ and $w_2^{(0)}$ and compute $V^{(0)}$ as the solution of the corresponding Poisson equation. Assign real numbers c, d, η, $\varepsilon > 0$, $\alpha^{(0)} \geq 0$, $\delta\alpha \geq 0$, and vectors $w_1^{(-1)}$, $w_2^{(-1)}$. Let $V^{(\ell)}$, $w_1^{(\ell)}$, $w_2^{(\ell)}$, and $\alpha^{(\ell)}$ be given. The Gummel-type iteration is as follows:

1. Set $V = V^{(\ell)}$, $v_1 = w_1^{(\ell)}$, and $v_2 = w_1^{(\ell)}$.
2. Set $V_1 = V + \delta V$, where δV is the solution of

$$\lambda^2\Delta(\delta V) - n(V,v_1,v_2)\delta V = -\lambda^2\Delta V + n(V,v_1,v_2) - C(x) \text{ in } \Omega, \tag{3.4}$$
$$\delta V = 0 \text{ on } \Gamma_D, \quad \nabla V\cdot\nu = 0 \text{ on } \Gamma_N, \tag{3.5}$$

   where $n(V,v_1,v_2)$ is defined in (2.1). If $\|\delta V\|_{L^\infty} \geq \max\{\varepsilon, c\|(w_1^{(\ell)},w_2^{(\ell)}) - (w_1^{(\ell-1)},w_2^{(\ell-1)})\|_{L^\infty}^d\}$ then set $V = V_1$ and repeat step 2; otherwise proceed with step 3.
3. Set $V = V_1$. Let w_1 and w_2 be the solutions of the linear system

$$-\operatorname{div} I_1 = 0, \quad I_1 = D_{11}\nabla w_1 + D_{12}\nabla w_2,$$
$$-\operatorname{div} I_2 + \sigma(v_2)w_2 = W_1(v_2), \quad I_2 = D_{21}\nabla w_1 + \Big(D_{22} + \frac{3}{2}\alpha n v_2^{-1}\Big)\nabla w_2,$$
$$w_1 = w_{D1},\ w_2 = w_{2D} \text{ on } \Gamma_D, \quad I_1\cdot\nu = I_2\cdot\nu = 0 \text{ on } \Gamma_N,$$

   where $D_{ij} = D_{ij}(V,v_1,v_2)$ and the boundary data are defined in (2.2).
4. Set $V^{(\ell+1)} = V$, $w_1^{(\ell+1)} = w_1$, $w_2^{(\ell+1)} = w_2$, and $\alpha^{(\ell+1)} = \alpha^{(\ell)} + \delta\alpha$. If $\|(w_1^{(\ell+1)}, w_2^{(\ell+1)}) - (w_1^{(\ell)},w_2^{(\ell)})\|_{L^\infty} \geq \eta$ then $\ell := \ell + 1$ and repeat step 1; otherwise stop.

The above linear systems are solved using the mixed finite-element discretization described in section 2. Gummel-type iteration schemes are very sensitive to the choice of initial data, in particular far from thermal equilibrium. Therefore, the above algorithm is coupled to a continuation in the applied bias (with uniform steps). Moreover, we have chosen for simplicity the damping parameter $\alpha^{(\ell)}$ to be independent of the solution. In numerical tests, we observed that the error tolerance in step 2 of the above algorithm has to be chosen rather small in order to achieve global convergence. The choice of the parameters is specified in section 4.

The second Gummel scheme consists in a decoupling of the current continuity equations by backward substitution according to (1.8)-(1.9):

Algorithm 2: Assign the starting values $w_1^{(0)}$ and $w_2^{(0)}$. Compute $V^{(0)}$ as the solution of the Poisson equation. Assign numbers c, d, η, $\varepsilon > 0$, $\alpha^{(0)} \geq 0$, $\delta\alpha \geq 0$, and vectors $w_1^{(-1)}$ and $w_2^{(-1)}$. Let $V^{(\ell)}$, $w_1^{(\ell)}$, $w_2^{(\ell)}$, and $\alpha^{(\ell)}$ be given.

1. Set $V = V^{(\ell)}$, $v_1 = w_2^{(\ell)}$, and $v_2 = w_2^{(\ell)}$.
2. Set $V_1 = V + \delta V$, where δV is the solution of the linear Poisson problem (3.4)-(3.5). If $\|\delta V\|_{L^\infty} \geq \max\{\varepsilon, c\|(w_1^{(\ell)},w_2^{(\ell)}) - (w_1^{(\ell-1)},w_2^{(\ell-1)})\|_{L^\infty}^d\}$ then set $V = V_1$ and repeat step 2; otherwise proceed with step 3.

3. Set $V = V_1$ and find δw_2 such that

$$-\mathrm{div}\,(\delta I_2) + \sigma(v_2)\delta w_2 = \mathrm{div}\,(D_{21}\nabla v_1 + D_{22}\nabla v_2) + W(V, v_1, v_2), \qquad (3.6)$$
$$\delta I_2 = \frac{3}{2} n v_2^{-2} \nabla(\delta w_2),$$

subject to the boundary conditions $\delta w_2 = 0$ on Γ_D and $(\delta I_2)\cdot\nu = 0$ on Γ_N, where $\sigma(v_2)$ is defined in (3.3), $n = n(V, v_1, v_2)$, and $D_{ij} = D_{ij}(V, v_1, v_2)$. Set $w_2 = v_2 + \delta w_2/(1+\alpha)$.

4. Set $V_1 = V + \delta V$, where δV is the solution of the linear Poisson problem (3.4)-(3.5) with v_2 replaced by w_2. If $\|\delta V\|_{L^\infty} \geq \max\{\varepsilon, c\|(w_1^{(\ell)}, w_2^{(\ell)}) - (w_1^{(\ell-1)}, w_2^{(\ell-1)})\|_{L^\infty}^d\}$ then set $V = V_1$ and repeat step 4; otherwise proceed with step 5.
5. Set $V = V_1$ and find w_1 such that

$$-\mathrm{div}\, I_1 = 0, \quad I_1 = D_{11}(V, w_1, w_2)\nabla w_1 + D_{12}(V, w_1, w_2)\nabla w_2,$$

subject to the boundary conditions $w_1 = w_{1D}$ on Γ_D and $I_1\cdot\nu = 0$ on Γ_N.
6. Set $V^{(\ell+1)} = V$, $w_1^{(\ell+1)} = w_1$, $w_2^{(\ell+1)} = w_2$, and $\alpha^{(\ell+1)} = \alpha^{(\ell)} + \delta\alpha$. If $\|(w_1^{(\ell+1)}, w_2^{(\ell+1)}) - (w_1^{(\ell)}, w_2^{(\ell)})\|_{L^\infty} \geq \eta$ then $\ell := \ell + 1$ and repeat step 1; otherwise stop.

Although the right-hand side of the decoupled equation (3.6) is only an H^{-1} function, the above algorithm worked well in the numerical simulations. Notice that the order in which we solve the linear problems matters. If we would solve the equation for v_1 first and then that for v_2, the algorithm did not work.

Both iterative schemes are combined with vector extrapolation. Let $x_0 = (w_1^{(\ell)}, w_2^{(\ell)})$ be a discrete solution defined by step 4 of Algorithm 1 or by steps 3 and 5 of Algorithm 2. We generate a finite sequence $x_j = (w_1^{(\ell+j)}, w_2^{(\ell+j)})$, $j = 1, \ldots, K$, and apply reduced rank extrapolation to these vectors [32]. More precisely, we introduce the following algorithm:

1. Set $s_0 = (w_1^{(\ell)}, w_2^{(\ell)})$, $j = 0$, and let $K \in \mathbb{N}$ be given.
2. Set $j := j + 1$ and compute $(w_1^{(\ell+j)}, w_2^{(\ell+j)})$ by applying Algorithm 1 or 2. If $\|(w_1^{(\ell+j)}, w_2^{(\ell+j)}) - (w_1^{(\ell+j-1)}, w_2^{(\ell+j-1)})\|_{L^\infty} \leq \eta$ or $j \geq K$ then stop and proceed with step 3; otherwise, repeat step 2.
3. Apply reduced rank extrapolation according to [32] to compute a vector (w_1^*, w_2^*).
4. Set $s_i = (w_1^*, w_2^*)$, $i := i + 1$, replace $(w_1^{(\ell)}, w_2^{(\ell)})$ by (w_1^*, w_2^*) and return to step 2.

The number K of base sequence vectors is related to the number of "dominant" eigenvalues of the linearization of the fixed-point map (see [32]). We still have to make clear how K is chosen. In the simulations, a value of K is accepted if the least-square residuals are smaller than 10^{-8}, a value which proved to be useful. In the reduced rank extrapolation, usually a pseudo-inverse has to be computed. Instead we have solved the corresponding least-square problem.

The reduced rank extrapolation can be also applied to the vector sequences generated in the inner iteration for solving the Poisson equation (step 2 of Algorithm 1). The number of base sequence vectors of this inner iteration will be denoted by K_1. This iteration is actually needed for the algorithm to be implementable. The global convergence of this modified algorithm is accelerated if carefully designed. Since the

convergence of the global iteration is very sensitive to the convergence of this inner iteration, generally a large number of vectors x_j has to be generated to ensure rapid convergence of the extrapolated values. On the other hand, the number of these vectors should not be chosen too large, since in each inner cycle a large linear system has to be solved.

3.3. Remarks on the implementation. In this subsection, we give some details of the numerical implementation. More details can be found in [18]. The source code of the algorithm is implemented in MATLAB. The 3D grid is generated by FEMLAB. The linear problems, occuring in Algorithms 1 and 2 above, are solved with a preconditioned conjugate gradient method. An incomplete Cholesky factorization with a problem-dependent drop tolerance is used as preconditioner. The MATLAB command `cholinc` realizes this factorization. The extension V_A of the applied voltage U (see (3.1)) is computed by means of the preconditioned conjugate gradient method employing the same preconditioner as mentioned before.

The matrices arising in both the Newton and the Gummel-type methods are generally badly conditioned, in particular for three-dimensional domains. A simple scaling of rows and columns improves the condition of the system. The Jacobian is scaled by dividing each row by the corresponding diagonal entry, which is assumed to be nonzero. For the Gummel-type methods, we multiply the rows and columns by the square root of the diagonal entry, which is generally positive. This allows to retain the symmetry and positive definiteness of the matrix.

For the integration of the doping profile $C(x)$ on the elements K of the triangulation $\mathcal{T}_h$, we employ an adaptive Simpson quadrature, provided by the MATLAB command `triplequad`, together with an appropriate transformation to K. The convergence of the iterative methods can be improved by smoothing the doping profile. More precisely, for all $K \in \mathcal{T}_h$, we average the approximations $C_K = \int_K C(x)dx$ with those of the neighboring tetrahedra, yielding $\overline{C}_K$. This ensures that the smoothing depends on the mesh parameter h such that for $h \to 0$, it holds

$$\sum_{K\in\mathcal{T}_h} \overline{C}_K \to \int_\Omega C(x)dx.$$

For the path-following method, we employ a constant step size $\tau = \tau^{(k)}$ (specified in section 4). Furthermore, we choose $\gamma = \gamma^{(k)} = 1$ and

$$c = c^{(k)} = -(\underbrace{\overline{c}/N, \ldots, \overline{c}/N}_{2N \text{ entries}}, \underbrace{0, \ldots, 0}_{N \text{ entries}})^\top,$$

where N denotes the degrees of freedom and $\overline{c}$ is a positive number independent of N whose value varies with the simulations. If $c = 0$, the step control reduces to the method of continuation in the applied bias with an increment which is only controlled by the step size τ.

4. Numerical examples. We present simulations of silicon metal-semiconductor field-effect transistors (MESFETs) in two and three space dimensions using the discretization and the iterative schemes described in the previous sections. MESFETs are voltage-driven devices which are used as a switch or amplifier. They consist of two highly-doped n^+ regions near the Ohmic contacts (called source and drain) and an n region with one or several Schottky contacts (called gates) in a sandwich configuration. The behavior of the device is mainly governed by the size of the depletion region (a

region with very low electron density) that develops around the Schottky contacts. The depletion region enlarges if the gate voltage is decreased and therefore diminishes the channel width leading to a reduced current for a fixed applied drain voltage (closed state). For a larger gate voltage, the depletion region becomes smaller and a significant current can flow (open state).

4.1. 2D double-gate MESFET. The model parameters of the silicon MESFET of size $0.6\,\mu\text{m}\times 0.24\,\mu\text{m}$ are taken from [21] for comparison (see Figure 4.1). The source and drain contact lengths are $0.24\,\mu$m; the gate length is $0.2\,\mu$m. The length of the low doped (channel) region is $0.36\,\mu$m. The doping profile takes the value $3\cdot 10^{17}\,\text{cm}^{-3}$ in the n^+-regions and $10^{17}\,\text{cm}^{-3}$ in the channel. At the source and drain, the particle density is equal to the equilibrium density [24]. The boundary values for the potential at the Ohmic contacts are the sum of the built-in potential V_{bi} and the applied voltage. At the Schottky contacts, the Schottky barrier height is substracted, i.e., $V_{|\text{Gate}} = U + V_{\text{bi}} - V_B$. A barrier height of 0.8 V is used as a typical value for an n-type silicon-metal contact. The temperature at the contacts is equal to the ambient temperature of 300 K. The particle density at the Schottky contacts is computed from formula (5.1-19) in [31]. Thus, the Dirichlet boundary conditions read as follows:

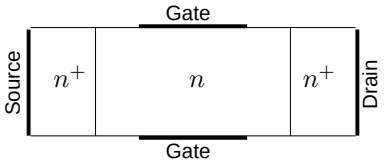

FIG. 4.1. *Geometry of the 2D double-gate MESFET.*

- at the source: $n = 3\cdot 10^{17}\,\text{cm}^{-3}$, $V = V_{\text{bi}}$;
- at the drain: $n = 3\cdot 10^{17}\,\text{cm}^{-3}$, $V = V_{\text{bi}} + 2\,\text{V}$;
- at the gates: $n = 3.9\cdot 10^{5}\,\text{cm}^{-3}$, $V = 0\,\text{V} + V_{\text{bi}} - 0.8\,\text{V}$ (open state),
  $n = 2.4\cdot 10^{5}\,\text{cm}^{-3}$, $V = -1.2\,\text{V} + V_{\text{bi}} - 0.8\,\text{V}$ (closed state).

The remaining physical parameters are as in [21] except for the energy relaxation time which equals $\tau_0 = 10^{-13}\,\text{s}$.

We have applied the Gummel-type schemes (Algorithms 1 and 2) and the full Newton method (combined with path following). For the Newton scheme, we have used the following parameters: $\overline{c} = 0.125$, $\tau = 0.02$ (open state) or $\overline{c} = 0.05$, $\tau = 0.008$ (closed state). For the Gummel-type schemes, it holds: $\delta\alpha = 0.5$, $c = 10^{-5}$, $d = 0.7$, $\eta = 10^{-6}$, $\varepsilon = 10^{-9}$, and $K_1 = 15$. For Algorithm 1 (or 2), we have chosen $\alpha^{(0)} = 5$ ($\alpha^{(0)} = 20$), and $K = 50$ ($K = 80$). We recall that the parameters $\overline{c}$ and τ are needed for the path-following method, c, d, η, ε determine the tolerances of the Gummel iterations, $\delta\alpha$ and $\alpha^{(0)}$ determine the damping in the Gummel iterations, and K and K_1 are the number of base sequence vectors for the vector extrapolation in the global and inner iterations, respectively.

In Figure 4.2 (left) the effect of the path-following method used in the Newton scheme is shown for an open state MESFET. For small applied voltage (i.e., the number of continuation steps is small), the step control reduces the voltage step, whereas the voltage step is allowed to be larger far from thermal equilibrium. The dashed line indicates the value of ρ when no step control is active, i.e., the voltage is uniformly increased according to (3.2) with $c = 0$ and $\tau = 0.025$. In closed state, the

step control suggests smaller values for ρ compared to the uniform voltage step (see Figure 4.2, right). Due to the enlarged depletion region, in which the electron density is rather small, more continuation steps are necessary.

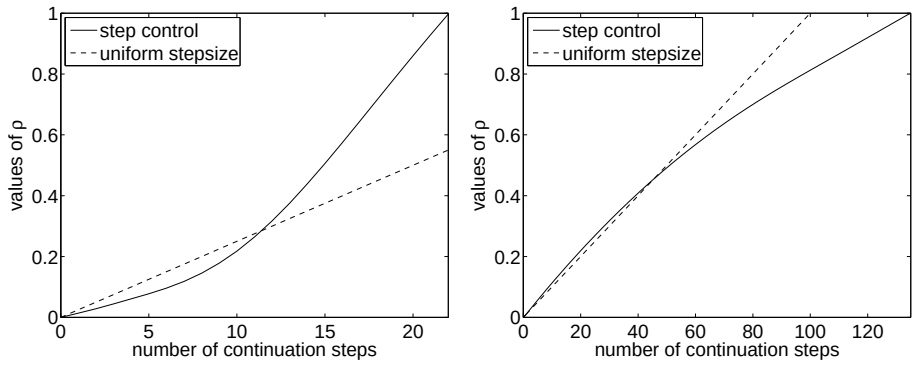

FIG. 4.2. *Effect of the path-following method on the voltage step. Left: open state; right: closed state.*

Figure 4.3 shows the absolute error in the discrete L^∞ norm depending on the number of Newton cycles. After four cycles, the error tolerance of 10^{-6} is achieved, independently of the step control parameter ρ (if $\rho < 1$). For comparison, the absolute errors for the Gummel-type algorithms, combined with vector extrapolation, are presented in Figure 4.4. The convergence of Algorithm 1 (left) seems to be only linear, whereas that of Algorithm 2 is superlinear (even quadratic). Quadratic convergence is expected if the number of base sequence vectors in the vector extrapolation method is close to the number of "dominant" eigenvalues. It seems that the number of dominant eigenvalues varies over a wide range for Algorithm 1, and this may cause the suboptimal linear convergence.

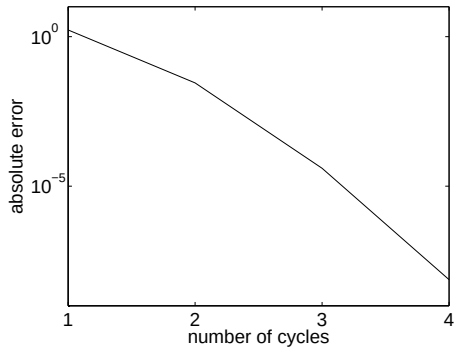

FIG. 4.3. *Convergence of the full Newton method (open state).*

The relative errors in the L^2 norm of the variables computed from the Newton scheme are presented in Table 4.1. Here, $\ell^* = 6.462 \cdot 10^{-5}$ cm is the device diameter, and the reference solution is computed on a fine grid with $h/\ell^* = 0.0025$. The temperature T_h is obtained by linear interpolation from $-1/w_2$. The values are verifying the quadratic convergence behavior.

In Figure 4.5 the electron density, temperature, and energy density are shown. We see that the electron density becomes very small in the depletion region near the

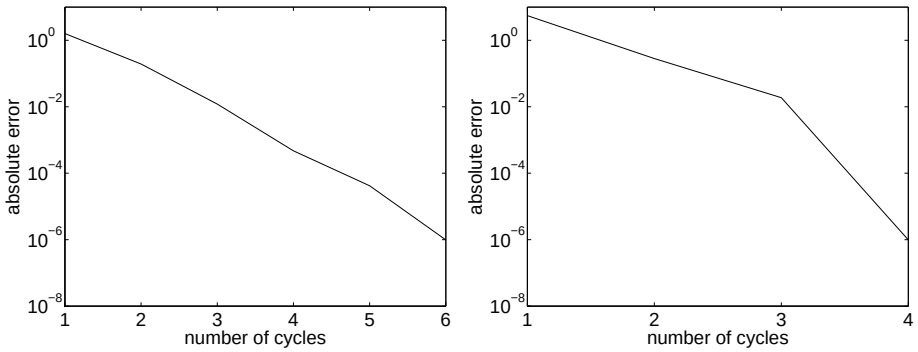

FIG. 4.4. *Convergence of the Gummel-type methods. Left: Algorithm 1, right: Algorithm 2 (open state).*

h/ℓ^*	RE for V_h	RE for w_{1h}	RE for w_{2h}	RE for T_h
0.08	0.071	0.065	0.120	0.110
0.04	0.033	0.039	0.081	0.058
0.02	0.035	0.021	0.051	0.047
0.01	0.0062	0.011	0.032	0.024

TABLE 4.1
Relative errors computed from the Newton method.

gate contacts. In open state, we can clearly observe the channel between the depletion regions. The velocity of the electrons, which travel from left to right, is significantly reduced when the electrons enter the drain region. The kinetic energy is transformed into thermal energy which explains the temperature rise at the end of the channel. Since the number of high-temperature electrons in the channel is rather small, the energy density is large in the source and drain regions in which the temperature is small but the number of electrons is large.

Finally, the electron current density is presented in Figure 4.6. There is a small current flow through the channel even in the closed state (right figure), but the current is significantly larger in the open state (left figure). In fact, the maximal drain current in closed state is only $6.3 \cdot 10^{-8}$ A. In a single-gate MESFET with the same geometry, the maximal drain current equals $7.6 \cdot 10^{-5}$ A which is much larger than the value for the double-gate device. This shows that the double-gate MESFET is more efficient in the closed state than a single-gate device.

4.2. Quasi-2D double-gate MESFET. The quasi-2D MESFET is a three-dimensional device which is uniform in one direction (see Figure 4.7). We have used a similar geometry like the 2D MESFET of section 4.1 such that the results of the 3D simulation can be compared with the 2D simulation. The values for the doping profile and the boundary conditions are as in section 4.1 for the open state. For the Gummel-type algorithms, we have chosen the following values: $c = 0.01$, $d = 0.7$, $\eta = 0.001$, $\varepsilon = 10^{-6}$, $K = 150$, $K_1 = 15$, $\alpha^{(0)} = 2$, $\delta\alpha = 2$ (Algorithm 1), and $\alpha^{(0)} = 15$, $\delta\alpha = 3$ (Algorithm 2).

The particle density, temperature, and energy density are depicted in Figure 4.8 for the open-state case. We see that the values are uniform in the z-direction. The values are similar to those for the 2D MESFET.

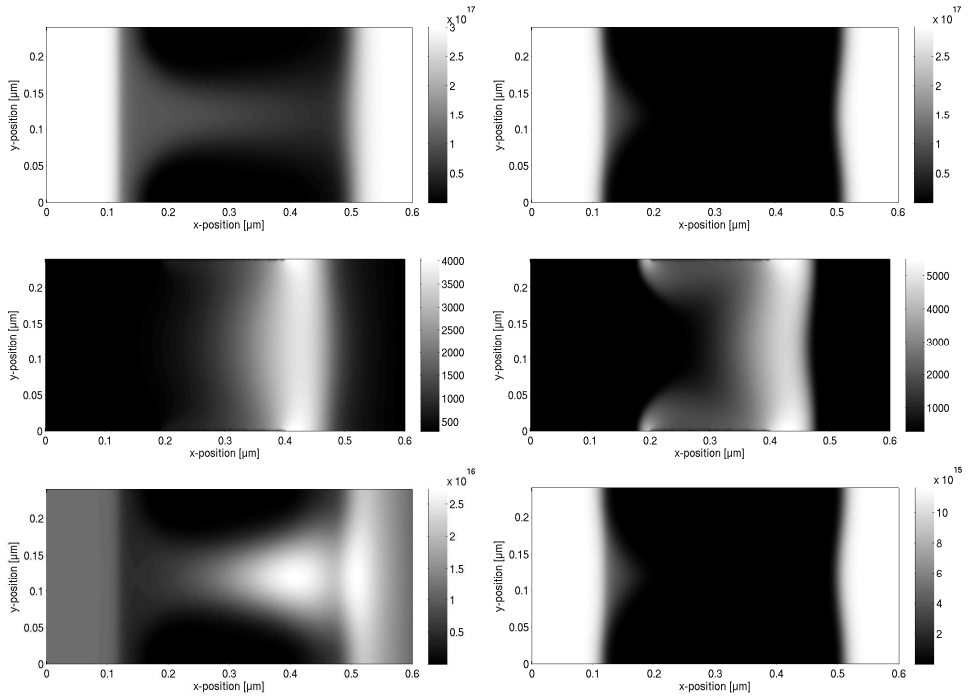

FIG. 4.5. *Electron density n in cm^{-3} (first row), electron temperature T in K (middle row), and energy density $\frac{3}{2}nT$ in $eV\,cm^{-3}$ (last row) for the double-gate MESFET in open state (left column) and in closed state (right column).*

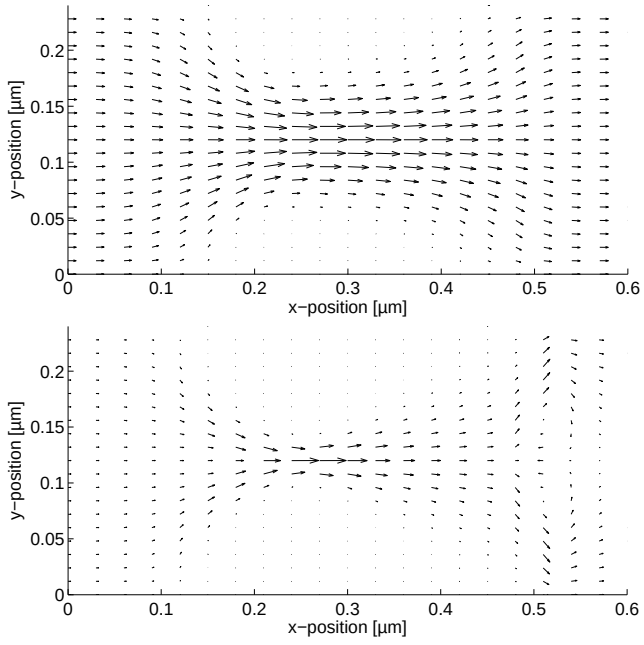

FIG. 4.6. *Electron current density in open (top) and closed state (bottom).*

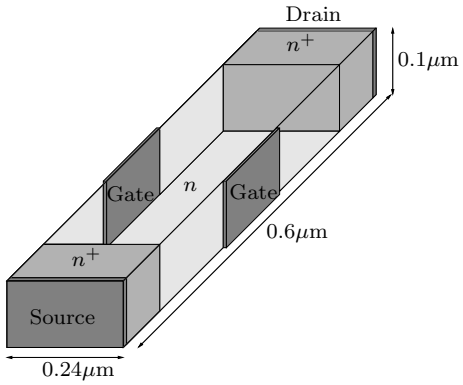

FIG. 4.7. *Geometry of the quasi-2D double-gate MESFET.*

4.3. 3D gate-all-around MESFET. The gate-all-around MESFET is a true 3D device since the gate is on all four sides of the transistor. This geometry allows for a very efficient switching behavior. The geometry of the device is shown in Figure 4.9. The channel length is $0.4\,\mu$m; the gate length is $0.33\,\mu$m. The source and the drain regions are highly doped with $3\cdot10^{18}\,\mathrm{cm}^{-3}$, and the channel is doped with $10^{18}\,\mathrm{cm}^{-3}$. The boundary conditions for the open state are similar as for the 2D MESFET of section 4.1, i.e., the temperature equals 300 K at all contacts and

- at the source: $n = 3\cdot10^{18}\,\mathrm{cm}^{-3}$, $V = V_{\mathrm{bi}}$;
- at the drain: $n = 3\cdot10^{18}\,\mathrm{cm}^{-3}$, $V = V_{\mathrm{bi}} + 2\,\mathrm{V}$;
- at the gates: $n = 3.9\cdot10^{5}\,\mathrm{cm}^{-3}$, $V = V_{\mathrm{bi}} - 0.8\,\mathrm{V}$.

We have employed the same iteration parameters as in section 4.2 except $\alpha^{(0)} = 5$ and $\tau = 0.0133$ for Algorithm 1.

The particle density, temperature, and energy density are depicted in Figure 4.10. The electron density is larger in the middle of the channel than close to the gate contacts since the transistor operates in the open state. These electrons contribute to the thermal energy which is large at the end of the channel region.

The current-voltage characteristic for the MESFET is presented in Figure 4.11. The current increases rapidly with the voltage and saturates for voltages larger than about 1 V. The current flow is smaller close to the gate contacts than in the middle of the channel due to the depletion region (Figure 4.12).

4.4. 3D single-gate MESFET. As final example we present some simulations for a 3D non-uniform single-gate MESFET of size $1\,\mu\mathrm{m}\times0.55\,\mu\mathrm{m}\times0.42\,\mu\mathrm{m}$. The geometry is adapted from [1] (see Figure 4.13). The n^+-region is doped with $5\cdot10^{17}\,\mathrm{cm}^{-3}$ and surrounded by a lightly doped substrate with doping $5\cdot10^{15}\,\mathrm{cm}^{-3}$. The temperature at the contacts equals 300 K, and the remaining boundary conditions are as follows:

- at the source: $n = 5\cdot10^{17}\,\mathrm{cm}^{-3}$, $V = V_{\mathrm{bi}}$;
- at the drain: $n = 5\cdot10^{17}\,\mathrm{cm}^{-3}$, $V = V_{\mathrm{bi}} + 2\,\mathrm{V}$;
- at the gates: $n = 3.9\cdot10^{5}\,\mathrm{cm}^{-3}$, $V = V_{\mathrm{bi}} - 0.8\,\mathrm{V}$.

For the Gummel schemes, we have employed the same parameters like in section 4.2 except $\alpha^{(0)} = 5$, $\tau = 0.0133$, and $K_1 = 25$.

The physical variables are shown in Figure 4.14. Due to the depletion region, the electron density is rather small close to the gate. The temperature is again large at the end of the channel. The current flow is large in the region between the source

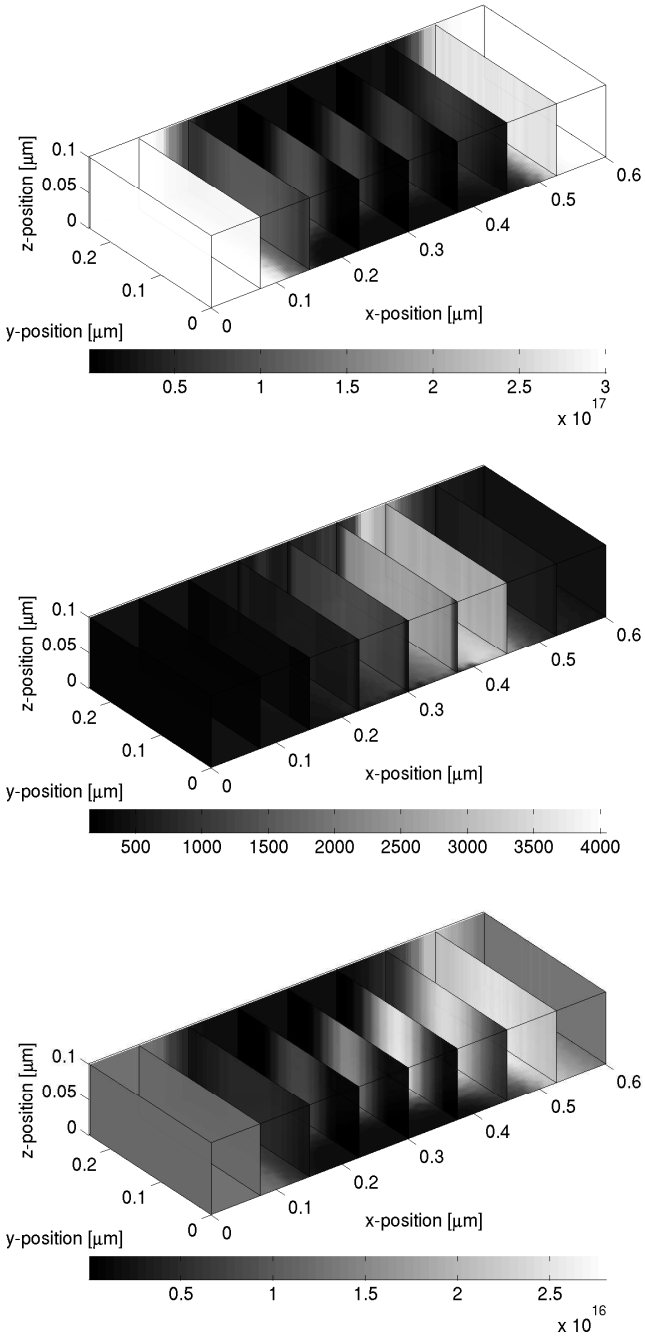

FIG. 4.8. *Electron density n in cm^{-3} (top), electron temperature T in K (middle), and energy density $\frac{3}{2}nT$ in $eV\,cm^{-3}$ (bottom) in the quasi-2D double-gate MESFET.*

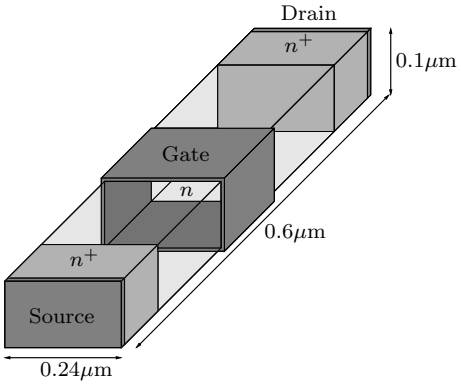

FIG. 4.9. *Geometry of the 3D gate-all-around MESFET.*

and gate contact since the electrons are accelerated from the electric field (see Figure 4.15). In fact, the current flow shows a true three-dimensional behavior.

5. Conclusion. In this paper we have discretized the 3D stationary energy-transport equations for semiconductors in the dual-entropy formulation by using Raviart-Thomas mixed finite elements. The main feature of the numerical scheme is the current conservation, in the sense that the jump of the normal component of the current at the inter-element boundaries vanishes.

Three iteration schemes are proposed: a full Newton method, combined with an adaptive voltage stepping computed by a path-following technique, and two Gummel-type methods, combined with reduced rank extrapolation. Although the Gummel-type schemes need more iteration cycles than the Newton method, they are more flexible from a programming view point. Moreover, the vector extrapolation technique allows to improve their convergence properties. In particular, the completely decoupled scheme converges superlinearly.

Various two- and three-dimensional MESFET transistors are numerically simulated, verifying the good properties of the numerical schemes. Our approach allows to simulate modern complex 3D structures which are becoming of increasing importance in the near future. Future research is concerned with the coupling of the energy-transport equations with a heat equation for the lattice temperature, which models the transfer of the thermal energy of the charge carriers to the semiconductor crystal.

REFERENCES

[1] S. ABOUD, J. BRANDLARD, S. GOODNICK, AND M. SARANITI, *Frequency analysis of 3D GaAs MESFET structures using full-band particle-based simulations*, J. Comput. Electr., 2 (2003), pp. 213–217.

[2] Y. APANOVICH, P. BLAKEY, R. COTTLE, E. LYUMKIS, B. POLSKY, A. SHUR, AND A. TCHERNIAEV, *Numerical simulations of submicrometer devices including coupled nonlocal transport and nonisothermal effects*, IEEE Trans. Electr. Dev., 42 (1995), pp. 890–897.

[3] D. ARNOLD AND F. BREZZI, *Mixed and nonconforming finite element methods: implementation, postprocessing and error estimates*, Math. Model. Numer. Anal., 19 (1985), pp. 7–32.

[4] N. BEN ABDALLAH AND P. DEGOND, *On a hierarchy of macroscopic models for semiconductors*, J. Math. Phys., 37 (1996), pp. 3308–3333.

[5] N. BEN ABDALLAH, L. DESVILLETTES, AND S. GÉNIEYS, *On the convergence of the Boltzmann equation for semiconductors towards an energy transport model*, J. Statist. Phys., 98 (2000), pp. 835–870.

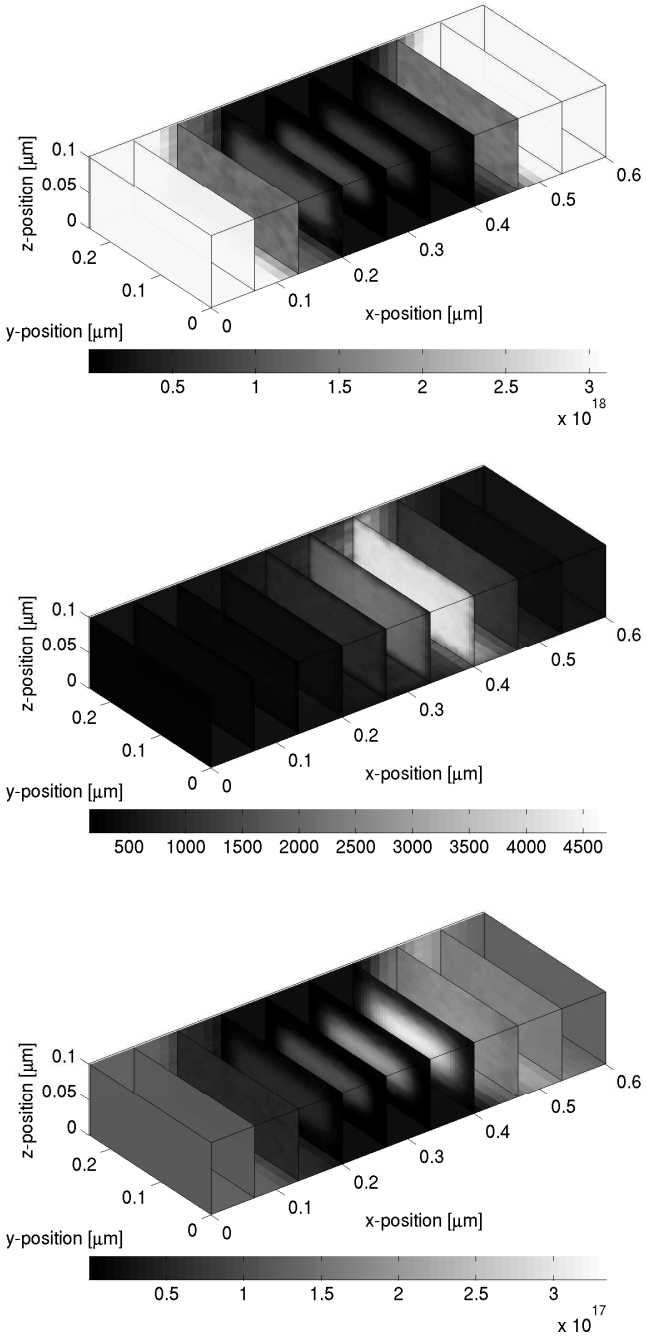

FIG. 4.10. *Electron density n in cm^{-3} (top), electron temperature T in K (middle), and energy density $\frac{3}{2}nT$ in $eV\,cm^{-3}$ (bottom) in the 3D gate-all-around MESFET.*

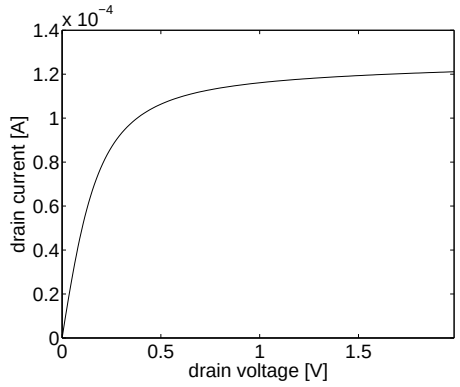

FIG. 4.11. *Current-voltage characteristic of the 3D gate-all-around MESFET.*

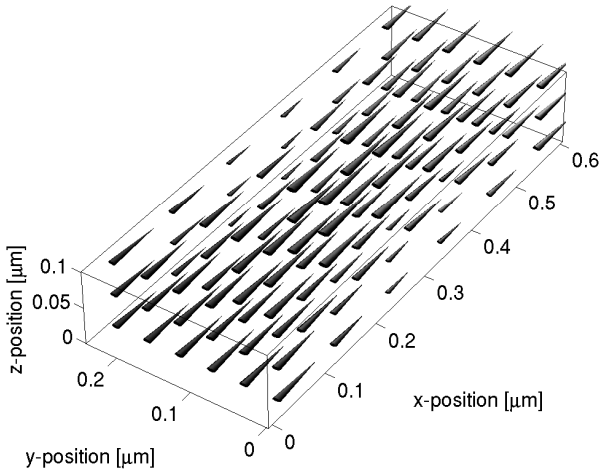

FIG. 4.12. *Electron current density in the 3D gate-all-around MESFET.*

[6] F. BOSISIO, R. SACCO, F. SALERI, AND E. GATTI, *Exponentially fitted mixed finite volumes for energy balance models in semiconductor device simulation*, in Proceedings of ENUMATH 97, H. Bock et al., eds., World Scientific, Singapore, 1998, pp. 188–197.

[7] F. BREZZI AND M. FORTIN, *Mixed and Hybrid Finite Element Methods*, Springer, New York, 1991.

[8] F. BREZZI, L. D. MARINI, S. MICHELETTI, P. PIETRA, R. SACCO, AND S. WANG, *Discretization of semiconductor device problems*, in Numerical Methods for Electrodynamical Problems, Handbook Numer. Anal., W. Schilders and E. ter Maten, eds., North–Holland, Amsterdam, 2005, pp. 317–441.

[9] F. BREZZI, L. D. MARINI, AND P. PIETRA, *Two-dimensional exponential fitting and applications to drift-diffusion models*, SIAM J. Numer. Anal., 26 (1989), pp. 1342–1355.

[10] P. CAUSSIGNAC, *An energy-transport model for semiconductor heterostructure devices: application to AlGaAs/GaAs MODFETs*, COMPEL, 18 (1999), pp. 61–76.

[11] D. CHEN, E. KAN, U. RAVAIOLI, C. SHU, AND R. DUTTON, *An improved energy transport model including nonparabolicity and non-Maxwellian distribution effects*, IEEE Electr. Dev. Letters, 13 (1992), pp. 26–28.

[12] P. DEGOND, S. GÉNIEYS, AND A. JÜNGEL, *A system of parabolic equations in nonequilibrium thermodynamics including thermal and electrical effects*, J. Math. Pures Appl., 76 (1997), pp. 991–1015.

[13] P. DEGOND, S. GÉNIEYS, AND A. JÜNGEL, *A steady-state system in nonequilibrium thermodynamics including thermal and electrical effects*, Math. Methods Appl. Sci., 21 (1998), pp.

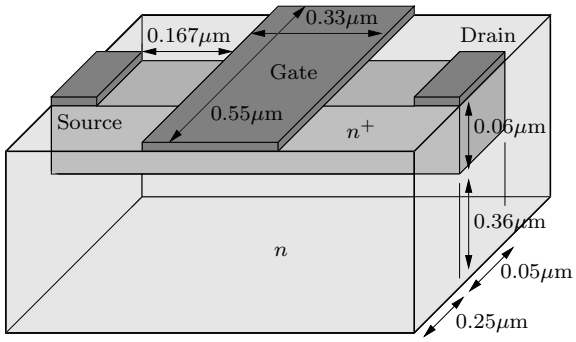

FIG. 4.13. *Geometry of the 3D non-uniform single-gate MESFET.*

1399–1413.

[14] P. DEGOND, A. JÜNGEL, AND P. PIETRA, *Numerical discretization of energy-transport models for semiconductors with non-parabolic band structure*, SIAM J. Sci. Comp., 22 (2000), pp. 986–1007.

[15] W. FANG AND K. ITO, *Existence of stationary solutions to an energy drift-diffusion model for semiconductor devices*, Math. Models Methods Appl. Sci., 11 (2001), pp. 827–840.

[16] C. FITZSIMONS, J. MILLER, S. WANG, AND C. WU, *Hexahedral finite elements for the stationary semiconductor device equations*, Comp. Meth. Appl. Mech. Engin., 84 (1990), pp. 43–57.

[17] A. FORGHIERI, R. GUERRIERI, P. CIAMPOLINI, A. GNUDI, M. RUDAN, AND G. BACCARANI, *A new discretization strategy of the semiconductor equations comprising momentum and energy balance*, IEEE Trans. Comp. Aided Design Integr. Circuits Sys., 7 (1988), pp. 231–242.

[18] S. Gadau. *Finite-element Discretizations of 3D Energy-transport Equations for Semiconductors*. PhD Thesis, Universität Mainz, Germany, 2007.

[19] J. GRIEPENTROG, *An application of the implicit function theorem to an energy model of the semiconductor theory*, Z. Angew. Math. Mech., 79 (1999), pp. 43–51.

[20] S. HOLST, A. JÜNGEL, AND P. PIETRA, *A mixed finite-element discretization of the energy-transport model for semiconductors*, SIAM J. Sci. Comput., 24 (2003), pp. 2058–2075.

[21] S. HOLST, A. JÜNGEL, AND P. PIETRA, *An adaptive mixed scheme for energy-transport simulations of field-effect transistors*, SIAM J. Sci. Comput., 25 (2004), pp. 1698–1716.

[22] J. JEROME, *Analysis of Charge Transport. A Mathematical Study of Semiconductor Devices*, Springer, Berlin, 1996.

[23] J. JEROME AND C.-W. SHU, *Energy models for one-carrier transport in semiconductor devices*, in Semiconductors, Part II, IMA Vol. Math. Appl. 59, W. Coughran et al., eds., Springer-Verlag, New York, 1994, pp. 185–207.

[24] A. JÜNGEL, *Quasi-hydrodynamic Semiconductor Equations*, Birkhäuser, Basel, 2001.

[25] L. D. MARINI AND P. PIETRA, *An abstract theory for mixed approximations of second order elliptic problems*, Mat. Apl. Comput., 8 (1989), pp. 219–239.

[26] L. D. MARINI AND P. PIETRA, *New mixed finite element schemes for current continuity equations*, COMPEL, 9 (1990), pp. 257–268.

[27] A. MARROCCO, P. MONTARNAL, AND B. PERTHAME, *Simulation of the energy-transport and simplified hydrodynamic models for semiconductor devices using mixed finite elements*, in Proceedings of ECCOMAS 96, John Wiley, London, 1996.

[28] P. RAVIART AND J. THOMAS, *A mixed finite element method for second order elliptic equations*, in Mathematical Aspects of the Finite Element Method, vol. 606 of Lecture Notes in Math., Springer, 1977, pp. 292–315.

[29] C. RINGHOFER, *An entropy-based finite difference method for the energy transport system*, Math. Models Methods Appl. Sci., 11 (2001), pp. 769–796.

[30] H. SCHWETLICK, G. TIMMERMANN, AND R. LÖSCHE, *Path following for large nonlinear equations by implicit block elimination based on recursive projections*, in Lecture Appl. Math., 32 (1996), pp. 715–732.

[31] S. Selberherr, *Analysis and Simulation of Semiconductor Devices*, Springer, Vienna, 1984.

[32] D. SMITH, W. FORD, AND A. SIDI, *Extrapolation methods for vector sequences*, SIAM Review, 29 (1987), pp. 199–233.

[33] K. SOUISSI, F. ODEH, H. TANG, AND A. GNUDI, *Comparative studies of hydrodynamic and*

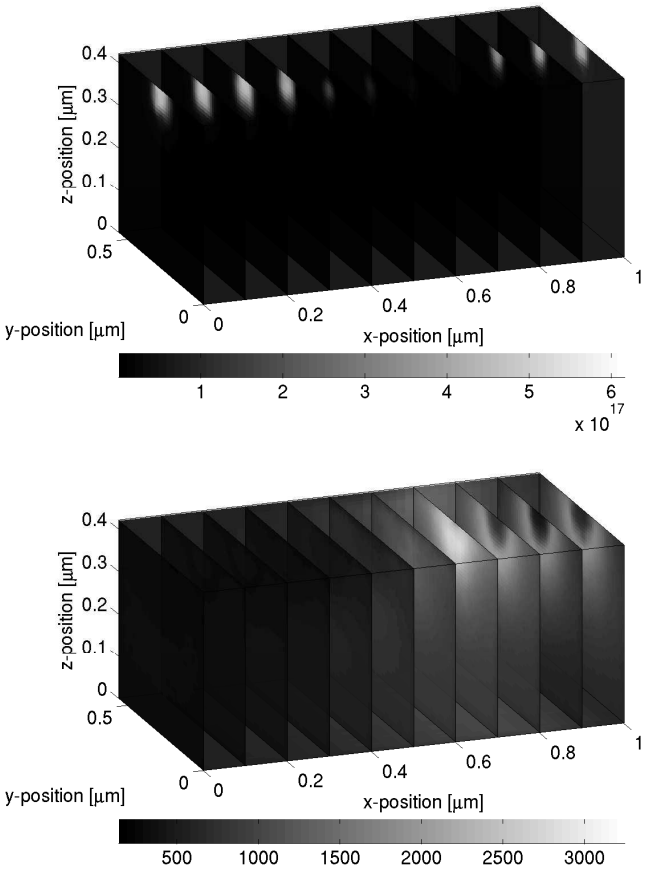

FIG. 4.14. *Electron density n in cm^{-3} (top) and electron temperature T in K (bottom) in the 3D non-uniform single-gate MESFET.*

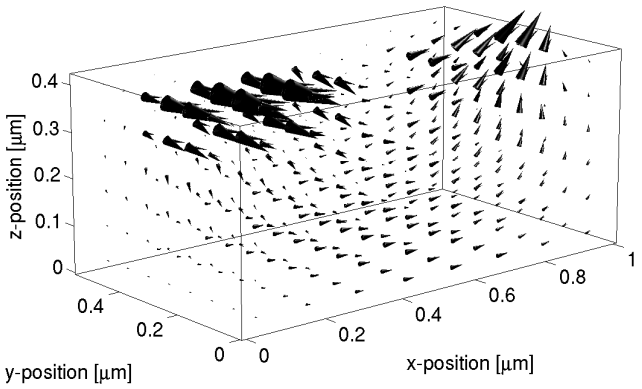

FIG. 4.15. *Electron current density in the 3D non-uniform single-gate MESFET.*

energy transport models, COMPEL, 13 (1994), pp. 439–453.
[34] R. Stratton, *Diffusion of hot and cold electrons in semiconductor barriers*, Phys. Rev., 126 (1962), pp. 2002–2014.